AGU ADVANCING EARTH AND SPACE SCIENCES

Geochemistry, Geophysics, Geosystems

RESEARCH ARTICLE

10.1029/2023GC011285

Implications of Surface Heat Flux for Shear Stress and Temperature on the Plate Interface Beneath Northern Honshu

Philip England[1], **Takumi Matsumoto**[2], **and Simon Wallis**[3]

[1]Department of Earth Sciences, University of Oxford, Oxford, UK, [2]National Research Institute for Earth Science and Disaster Resilience, Ibaraki, Japan, [3]Department of Earth and Planetary Science, Faculty of Science, The University of Tokyo, Tokyo, Japan

Key Points:

- Surface heat flux measurements constrain temperature (660 ± 240°C) and shear stress (100 ± 45 MPa) at ~60 km on the plate interface in N Honshu
- These values are supported by estimates from dense heat flux measurements at the Kermadec plate boundary (630 ± 140°C) and (115 ± 25 MPa)
- Metamorphic temperatures in an exhumed plate interface, the Sanbagawa belt of SW Japan, are also explained by this level of shear stress

Correspondence to:

P. England,
philip.england@earth.ox.ac.uk

Citation:

England, P., Matsumoto, T., & Wallis, S. (2024). Implications of surface heat flux for shear stress and temperature on the plate interface beneath northern Honshu. *Geochemistry, Geophysics, Geosystems*, *25*, e2023GC011285. https://doi.org/10.1029/2023GC011285

Received 6 OCT 2023
Accepted 7 JAN 2024

Author Contributions:

Conceptualization: Philip England, Takumi Matsumoto, Simon Wallis
Data curation: Takumi Matsumoto
Formal analysis: Philip England, Takumi Matsumoto
Investigation: Philip England
Methodology: Philip England, Takumi Matsumoto, Simon Wallis
Validation: Philip England, Takumi Matsumoto
Writing – original draft: Philip England
Writing – review & editing: Philip England, Takumi Matsumoto, Simon Wallis

Abstract Measurements of surface heat flux from boreholes of the NIED Hi-net network of seismometers are used to determine temperature and shear stress on the plate interface beneath northern Honshu. At the maximum depth of thrust-faulting earthquakes, about 60 km, the temperature is 660 ± 240°C and the average shear stress during slip on the interface is 100 ± 45 MPa. The equivalent quantities from the oceanic setting of the Kermadec trench are 630 ± 140°C and 115 ± 25 MPa. The shear stresses are substantially higher than commonly assumed in models of convergent plate interfaces, but are consistent with measurements made above other convergent plate interfaces where heat flux data are more sparse. They are also consistent with the level of shear stress required to explain measurements of pressure and temperature from high-pressure-low-temperature terrains that experienced metamorphism on subduction interfaces, in particular those from the Cretaceous Sanbagawa belt of SW Japan.

Plain Language Summary The temperatures and stresses under which most of the world's great earthquakes nucleate are poorly known because they take place at depths of tens of kilometers, where conditions cannot be directly observed. Measurements of surface heat flux above plate interfaces provide the strongest indirect constraints, but those measurements are sparse. We use a dense set of heat flux measurements to determine shear stress and temperature on the plate interface of northern Honshu, on which the 2011 Tōhoku earthquake occurred. The shear stress, 100 ± 45 MPa, and temperature, 660 ± 240°C, are significantly higher than previous estimates, but are supported by analysis of heat flux above the Kermadec plate interface—the only location where a comparable density of heat flux measurements has been used to estimate shear stress. Shear stresses of ~100 MPa can also account for the conditions of temperature and pressure recorded in rocks of the Sanbagawa belt of SW Japan, which are the exhumed remnants of an approximately 90-million-year-old plate interface. This concordance supports arguments that the Sanbagawa, and similar terrains around the world, record physical and chemical conditions relevant to the generation of earthquakes on present-day plate interfaces.

1. Introduction

Characteristic features of thrust-faulting earthquakes on plate interfaces vary markedly, both among different zones, and with depth along individual interfaces (e.g., Lay et al., 2012). Understanding of those variations depends on knowledge of the of temperatures and shear stresses at the depths on plate interfaces. Constraints on those quantities are also required in modeling the initiation and propagation of earthquake ruptures (e.g., Abercrombie & Rice, 2005; Brantut & Rice, 2011; Garagash, 2012; Lambert et al., 2021; Segall & Bradley, 2012; Viesca & Garagash, 2015).

Because the depths at which major and great earthquakes nucleate are inaccessible to direct observation, estimates of shear stress and temperature come from proxies, of which the most direct are measurements of surface heat flux above plate interfaces. However, only one such study was designed specifically for that purpose (Von Herzen et al., 2001). Estimates from other studies (e.g., Antriasian et al., 2019; Chi & Reed, 2008; England, 2018; Gao & Wang, 2014; Hamamoto et al., 2011; McCaffrey et al., 2008; Molnar & England, 1990; Tichelaar & Ruff, 1993; Yoshioka et al., 2013) are subject to considerable uncertainty because of unfavorable distributions of data.

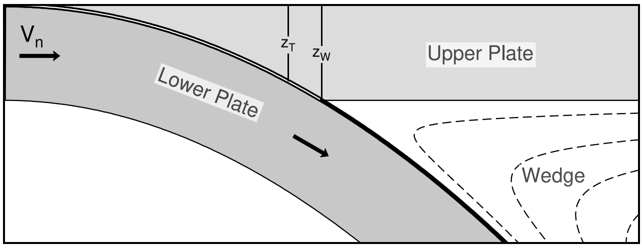

Figure 1. Definition sketch for this paper. The plate interface is shown by the double lines and the wedge-slab interface is shown by the thick line; the base of the plate interface is at depth z_W. Dissipative heating takes place from the surface to the depth z_T, which is assumed in this paper to be at the maximum depth of thrust-faulting earthquakes. Dashed lines schematically indicate streamlines of the fluid mantle wedge. The section is perpendicular to the trench, and V_n is the magnitude of the velocity, in that direction, of the lower plate relative to the upper plate.

The subduction interface consists of two principal segments (Figure 1). The plate interface is bounded by two rigid plates, within which heat transfer is dominated by diffusion perpendicular to the interface and advection parallel to it. Analytical expressions for the thermal structure of this segment (Molnar & England, 1990; England & May 2021, and Appendix A of this paper) provide the basis of our analysis. The wedge-slab interface is bounded by the descending lower plate and the mantle wedge; here heat transfer is dominated by advection and diffusion perpendicular to the interface. Uncertainties in analysis associated with the transition between these two regimes are discussed in Section 3.2.

We place a constraint on shear stresses on the plate interface beneath northern Honshu, and on temperatures at the seismic-aseismic transition on that interface, using a set of borehole heat flux measurements (Matsumoto et al., 2022). Although these data are limited to points on land, they cover regions in which the top of the slab is close to the maximum depth of thrust faulting on the interface, so constrain stresses and temperatures at that depth. These estimates have quite large uncertainties (~±250°C and ~±50 MPa) due to uncertainty in the rate of heat generation in the crust. We therefore compare estimates of shear stress and temperature beneath northern Honshu with those obtained from the data of Von Herzen et al. (2001) for the Kermadec plate interface, where the uncertainties are considerably smaller. Finally, we show that shear stresses of ~100 MPa, estimated for the present-day plate interfaces, explain the temperatures recorded in rocks of the Sanbagawa belt of SW Japan, which formed part of a convergent plate interface in Cretaceous time.

2. Data

2.1. Surface Heat Flux

We use the measurements of surface heat flux data made by Matsumoto et al. (2022), who describe the collection and analysis of temperatures and thermal conductivities from boreholes of the NIED Hi-net network of seismometers, which are at least 100 m in depth (Figure 2a). Of those data, we use only the heat flux measurements of Class A of Matsumoto et al. (2022); these show no evidence of non-conductive heat transfer below depths of 50 m (below 100 m in boreholes deeper than that). We concentrate on conditions at the maximum depth of thrust-faulting earthquakes, which is ~60 km beneath northern Honshu (e.g., Hayes et al., 2018; Heuret et al., 2011, and see Figure 2a), using surface heat flux measurements from sites beneath which the top of the slab is at depths between 50 and 70 km (histogram of Figure 2b). Seven further heat flux measurements are reported from sites within the region of interest for which boreholes penetrate beyond a few tens of meters (Tanaka et al., 2004) but no uncertainties are given, so we confine our attention to the data of Matsumoto et al. (2022).

2.2. Radiogenic Heat Production

Estimates of shear stress on the plate interface from measurements of surface heat flux above it are sensitive to the amount of radiogenic heat production beneath the surface (Section 3.2.2). Direct measurements of radiogenic heat production from rocks of the region are scarce, so we estimate the radiogenic heat production in the upper crust using a compilation of the chemical compositions of stream sediments from 3,000 catchments across Japan, made by Ohta et al. (2021), who show that these measurements are representative of the major rock types within each catchment from which the sediments were collected. We calculate the radiogenic heat production per unit volume, A, from the measured concentrations of potassium, thorium, and uranium (Ruedas, 2017) and display them in Figure 2c. The distribution of estimates of A from the 118 catchments beneath which the top of the slab lies at depths between 50 and 70 km is shown in Figure 2d. The principal near-surface rock types in the region covered in Figure 2d are sediments and sedimentary rocks, accretionary complex, and granites (Ohta et al., 2021, Figure 1). The average rates of heat production in those rock types, calculated from their average chemical compositions (Ohta et al., 2021, Table 5) are, respectively, 0.8, 1.0, and 1.7 μW m^{-3}. There are very few estimates of $A > 1.7$ μW m^{-3} in the region of interest (Figure 2d); we therefore take the average heat production in the granites to be a reasonable upper limit for the radiogenic heat production in the of the upper crust of the region.

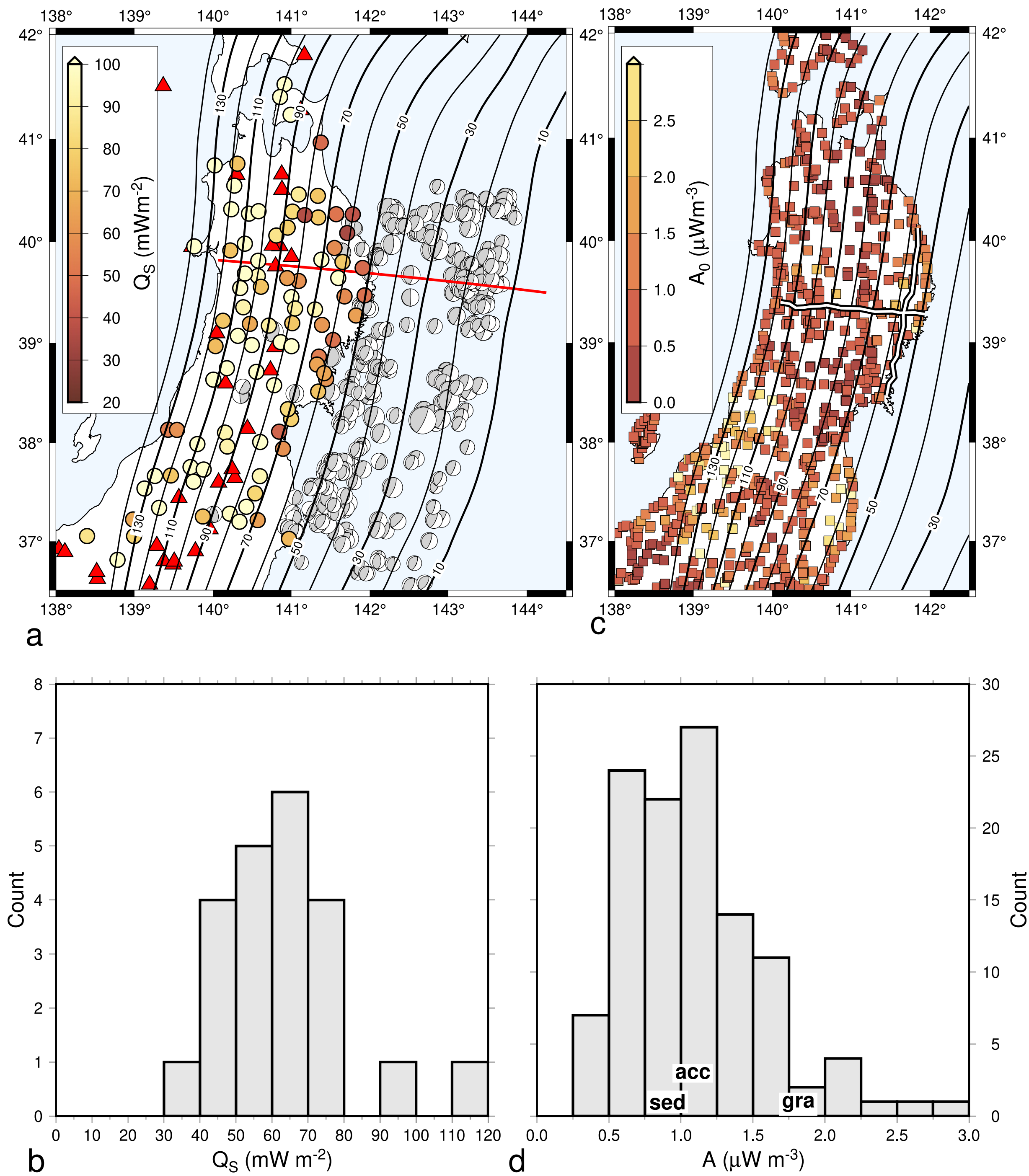

Figure 2. Surface heat flux and surface heat production in northern Honshu. (a) Distribution of heat flux measurements of Class A measured in NIED Hi-net boreholes (Matsumoto et al., 2022) (circles colored by the measured heat flux, scale to left). Red triangles show the locations of Holocene volcanoes (Venzke, 2023). Contours show depth to top of slab, in km (Hayes, 2018; Hayes et al., 2018). Gray symbols show focal mechanisms of reverse-faulting earthquakes from the GCMT catalog (Dziewonski et al., 1981; Ekström et al., 2012), with depths determined from the ISC-EHB catalog (Engdahl et al., 2020); the mechanisms shown are those whose hypocenters lie within 10 km of the top of the slab. The red line indicates the profile used by Gao and Wang (2014) and England (2018) in their analyses of heat flux in the region. (b) Surface heat flux measurements from locations beneath which the top of the slab lies between 50 and 70 km. (c) Estimates of average heat production of rocks calculated from geochemical measurements in catchments (Ohta et al., 2021) (Section 2.2). Double lines indicate the locations of seismic profiles of Iwasaki et al. (1994, 2001), on which estimates of thickness of upper and lower crust are based, (d) Estimates of surface heat production from locations beneath which the top of the slab lies between 50 and 70 km. Labels **sed**, **acc**, and **gra** indicate, respectively, the average heat production rates in **sed**iments and sedimentary rocks, sedimentary rocks of the **acc**retionary complex, and **gra**nitic rocks (Ohta et al., 2021, Table 5).

Seismic profiles approximately along the line of the 60-km contour of depth to the top of the slab (Iwasaki et al., 1994), and perpendicular to it (Iwasaki et al., 2001) (Figure 2c) show that the crust in the region of interest is about 30 km thick with a reflective lower crust that is about 15 km thick. A depth of ∼30 km for the Moho at this location is also supported by tomographic studies using natural seismicity (Matsubara et al., 2017). The lower crust is inferred, from comparison between P-wave speeds measured on the seismic profiles and those measured in the laboratory on lower crustal xenoliths of the region, to be gabbroic (Nishimoto et al., 2005). We assign a thickness of the layer to be 15 km, on the basis of seismic measurements of the thickness of the upper crust.

We take the rate of heat generation in the lower crust to be ∼0.2 μW m^{-3} (from the elemental abundances of Rudnick & Gao, 2003, Table 11); this level of heat generation would contribute a total of ∼3 mW m^{-2}, giving an estimate of 28.5 mW m^{-2} for the total heat generation in the crust, which we round to 30 mW m^{-2}. Radiogenic heat production in the oceanic lower plate is negligible in the present context. Our estimate of 30 mW m^{-2} for the total heat production per unit area in the upper plate, which we refer to as Q_A, matches that of Furukawa and Uyeda (1989), who based their estimate on measurements of heat production in an exhumed cross section of an island arc in Hokkaido, and on general considerations of heat production in felsic crust.

3. Shear Stress and Temperature on the Plate Interface Beneath Northern Honshu

3.1. Mathematical Model

We apply the mathematical model described in Appendix A to measurements of surface heat flux (Section 2.1) and radiogenic heat production (Section 2.2) in order to determine temperature and shear stress during slip on the plate interface beneath northern Honshu. This model, which applies to the two plates and the interface between them, neglects horizontal diffusion of heat in the upper plate and, within the lower plate, neglects diffusion parallel to the interface. The expressions resulting from this approximation are given in Appendix A and the notation is given in Table A1. These expressions agree with the results of numerical solutions to the full equations to within a few percent (England & May 2021; Molnar & England, 1990).

The temperature on the plate interface, T_f, is related to surface heat flux, Q_S, and radiogenic heat production per unit area in the crust, Q_A, by

$$T_f = \frac{z_f}{\overline{K}}\left[Q_S - Q_A\left(1 - \frac{\mathcal{D}}{2z_f}\right)\right]. \tag{1}$$

where z_f is depth of the plate interface, $\mathcal{D}$ is the length scale for distribution of heat production in the upper plate, and $\overline{K}$ is the average thermal conductivity of the upper plate (Equations 4, A1, and A12).

The shear stress during slip is related to heat flux and heat production by

$$\tau' = \frac{S_\tau}{V}\left[Q_S - Q_A\left(1 - \frac{\mathcal{D}}{2z_f}\left(1 - \frac{1}{S_A}\right)\right) - \frac{Q_0}{S_Q}\right], \tag{2}$$

where Q_0 is the surface heat flux appropriate to the age of the lower plate, V is convergence rate, and S_Q, S_τ, and S_A are divisors that express the fraction of each heat source that flows upwards through the upper plate (Appendix A; Equations A2, A10, and A12). We refer to τ' as the apparent shear stress to indicate that the heat flux measurements relate only to average shear stress during relative motion across the interface. Most of that motion takes place in large to great earthquakes (Scholz & Campos, 2012), and the apparent shear stress is likely to be much lower than the static shear stress (e.g., Rice, 2006). The apparent coefficient of friction, μ', on the plate interface is

$$\mu' = \frac{\tau'}{g\rho z_f}, \tag{3}$$

where g is the acceleration due to gravity and ρ is the average density of the plate above the interface. We are concerned with the region in which $z_f \sim 60$ km; approximately half that depth consists of continental crust and we take ρ to be 3,100 kg m^{-3}.

10.1029/2023GC011285

For each heat flux measurement we analyze, we set z_f to be the depth of the top of the slab beneath the point, and measure the distance u (which enters in the divisors S_A, S_Q, and S_τ) along the top of the slab in the up-dip direction from that point to the trench. The coordinates of the top of the slab are those of Slab2 (Hayes, 2018; Hayes et al., 2018) and those of the trench are from Bassett and Watts (2015). The speed of convergence, V, is obtained from the angular velocities of the Pacific and Okhotsk plates of Argus et al. (2011). The component of convergence in the direction normal to the trench, V_n, follows from the angle between the convergence direction and the dip direction. In the present case, that angle is small and the pole of relative motion is distant; V and V_n both lie in the range 89–93 mm/yr for all measurement points.

3.2. Uncertainties

3.2.1. Epistemic Uncertainty

Penniston-Dorland et al. (2015) discussed processes, in addition to dissipative heating, that could influence temperatures on the plate interface. Of these, they estimated that both circulation of rock and metamorphic reactions within the subduction channel could influence heat flux by $\sim 5 - 10$ mW m^{-2} (Penniston-Dorland et al., 2015, Figure 9). Although Shreve and Cloos (1986) consider that sediment circulation occurs in the plate interface beneath NE Japan, their model requires shear stress to be a few MPa, much smaller than the shear stress of ∼100 MPa estimated below; see England and Smye (2023, Sections 5 and 6) and Smye and England (2023, Section 4) for further discussion. The sign and magnitude of the contribution from metamorphic reactions are uncertain. If, as considered by Penniston-Dorland et al. (2015), there is pervasive hydration of mafic rock, then heat flux could be elevated by ∼10 mW m^{-2}, leading to overestimate of shear stress by ∼30 MPa. If, as discussed by Smye and England (2023, Section 3), there is pervasive dehydration, then shear stress obtained below would be underestimates.

The analytical approximation employed in this analysis (Equation A1) agrees to within ∼10°C with 2D numerical calculations of temperature on the plate interface (Molnar & England, 1990) and England and May (2021, Sections 2.4 and 2.5, and Figure 3). However, that approximation must break down as the plate interface approaches the wedge, whose thermal structure is dominated by advection of heat (Figure 1). We address the uncertainty associated with the approximate estimates of temperature and stress near the base of the plate interface by carrying out a numerical calculation that includes advection by flow in the wedge. Dissipation occurs from the surface to a depth of 60 km, the maximum depth of thrust-faulting earthquakes in the region (Figure 2). Slip without dissipation takes place from this depth to the base of the plate interface, which is taken to be at 75 km. Wada and Wang (2009) suggested that this choice of depth is reasonable on the grounds of fit to surface heat flux. Below 75 km, the lower plate is in contact with the mantle wedge. See Appendix B for further information.

There is no need to consider radiogenic heating in this comparison because its only influence would be a straightforward addition to the surface heat flux (Equation A12), which is then removed before estimating temperature (Equation 1) and apparent stress (Equation 2).

Although the temperature drops between 60 and 75 km on the plate interface, where there is no dissipative heating, the drop is not apparent in surface heat flux, Q_S, which varies little until the top of the lower plate approaches the mantle wedge at a depth of 75 km (Figure 3a). We use this profile of surface heat flux to calculate temperatures and shear stresses on the plate interface using the approximation expressions of Equation 1 and 2. Comparison of those estimates with the full solution (Figure 3) shows that errors introduced by the approximations when $z_f \sim 50 - 60$ km are of the order of 40–80°C in temperature and 10–15 MPa in apparent shear stress. If there is aseismic dissipation below the maximum depth of thrust-faulting earthquakes, those errors would be reduced.

3.2.2. Uncertainty in Parameters

Uncertainties in the estimates of apparent stress and temperature arise principally from uncertainties in the following parameters: the surface heat flux measurements, Q_S; the radiogenic heating per unit area, Q_A; the depth to the top of the slab, z_f, with corresponding uncertainty in the path length u to that depth; the thermal properties of the upper plate.

With two exceptions, the heat flux measurements we use (Figure 2b) have uncertainties of smaller than 10 mW m^{-2} (Matsumoto et al., 2022, Table 3). An uncertainty of 10 mW m^{-2} in Q_S is equivalent to an uncertainty of about 30 MPa in τ' (Equation 2, with $S_\tau \sim 10$), or of about 200°C in T_f (Equation 1). We estimate in Section 2.2

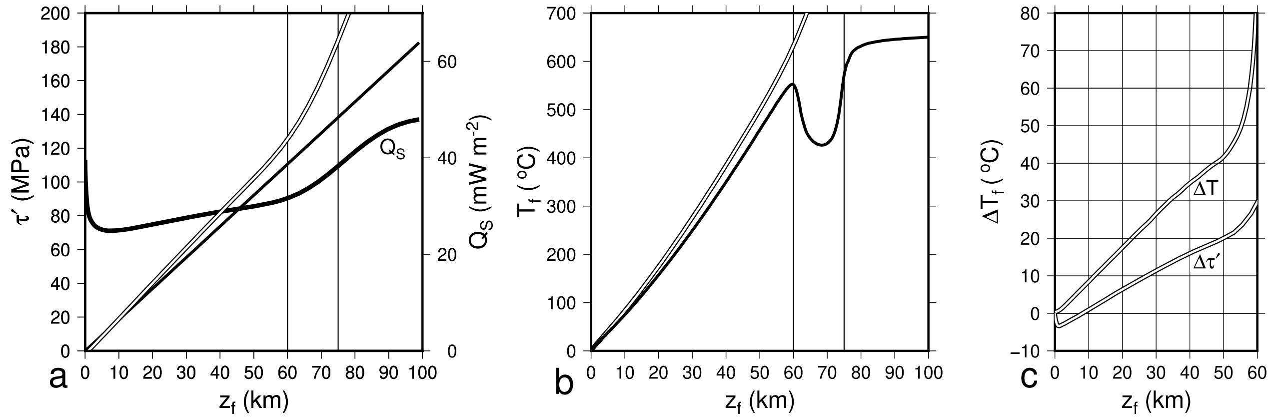

Figure 3. Test of the approximations used to estimate apparent shear stress and temperature on the plate interface against a 2D numerical calculation that includes advection of heat in the wedge corner (see text and Appendix B). Maximum depth of dissipation (60 km) and of the top of the wedge-slab interface (75 km) are shown by vertical lines. (a) Thicker solid line shows the distribution of surface heat flux, Q_S, from the numerical calculation; thinner solid line shows the effective shear stress, τ', on the interface. Double line shows τ' calculated from Q_S using the approximate expression of Equation 2. (b) Solid line shows temperature along the top of the slab in the numerical calculation. Double line shows the temperature calculated from the model Q_S using the approximate expression of Equation 1. (c) Differences, ΔT_f, $\Delta\tau'$ between the 1D approximate solutions (Equations 1 and 2) and the equivalent quantities in the 2D numerical calculations.

that $Q_A \sim 30$ mW m^{-2}. A change of 5 km in our estimate of the thickness of the heat-producing layer in the upper crust would change that parameter by 10 mW m^{-2}. Equally, if the rate of heat production in the neighborhood of a particular heat-flux measurement is closer to the mean for accretionary complex or sediments than it is to the granitic value we have assumed, then Q_A may be overestimated by ∼10 mW m^{-2}. We therefore adopt an uncertainty of 10 mW m^{-2} for the radiogenic contribution to surface heat flux, Q_A. As for Q_S, that uncertainty is equivalent to an uncertainty of 200°C in T_f and, with S_A in the present case being ∼6, to an uncertainty of about 30 MPa in τ', or 0.016 in μ' for $z_f = 60$ km.

We assign heat flux from the subducting plate, Q_0, using the expression of Parsons and Sclater (1977, Equation 23) for ocean floor of age 135 Myr, appropriate for the age of the Pacific plate beneath the measurement points. Q_0 appears in the expression for apparent shear stress (Equation 2), where its influence is reduced relative to those of Q_S and Q_A by the divisor S_Q; because $Q_0 \sim 40$ mW m^{-2} and S_Q is of order 10, even an error of 25% in Q_0 would be negligible in the present context.

Uncertainties in depth to the top of the slab for the region we consider are close to 15 km, or about 25% of the depth itself (Hayes, 2018; Hayes et al., 2018). Equation 1 shows that, because the term $\mathcal{D}/z_f$ is small, those uncertainties translate directly into ∼25% uncertainties in T_f. Similarly, because $S_\tau \gg 1$ so $S_\tau \propto z_f$, this source introduces ∼25% uncertainties in τ'.

Uncertainty in the averaged thermal conductivity of the upper plate, $\overline{K}$, influences estimates of temperature on the plate interface (Equation 1). To calculate that quantity, we assign nominal temperatures of 200°C to the base of the upper crust, and 400°C, and 600°C to the base of the crust and the plate interface, respectively. We then form estimates of the average conductivity of each layer over the temperature interval $T_1 \le T \le T_2$

$$\bar{k} = \frac{1}{(T_2 - T_1)} \int_{T_1}^{T_2} k(T')\,\mathrm{d}T', \tag{4}$$

where k is the temperature-dependent thermal conductivity assigned to the layer and $\bar{k}$ is its average for that layer. Plausible variation in the temperatures ranges over the different layers produce unimportant differences in estimates of their average conductivity; choice of the model for conductivity within the crust is the principal source of uncertainty. For the upper crust we use the expressions of Whittington et al. (2009), for the lower crust, that of Furlong and Chapman (2013) and for the upper mantle, that of Xu et al. (2004); these give average conductivities $\bar{k}$ of 3.7, 2.6, and 2.7 W m^{-1} K^{-1}, respectively, for those layers. With thicknesses of 15 km for each crustal layer, and 30 km for the mantle layer, the average thermal conductivity of the upper plate is 2.9 W m^{-1} K^{-1}. If the conductivity of the whole crust is calculated from the model of Whittington et al. (2009), $\overline{K}$ remains at

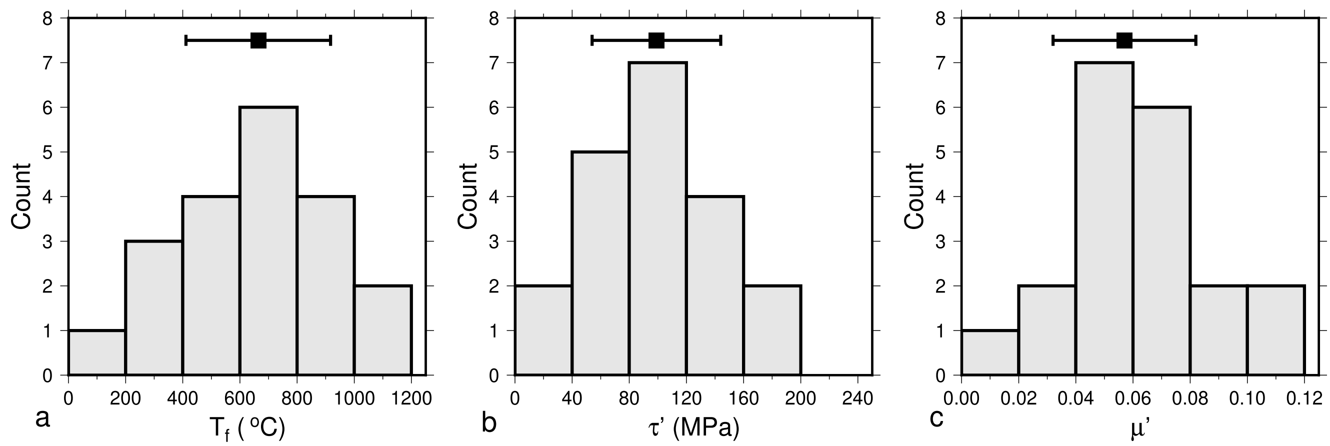

Figure 4. Estimates of temperature and apparent shear stress on the plate interface from heat flux measurements in NIED Hi-net boreholes (Matsumoto et al., 2022) situated above places where the top of the slab lies between 50 and 70 km (Figures 2a and 2b). (a) Temperature on the interface, calculated using Equation 1, as described in Sections 3.2.2 and 3.3. (b) Estimates of apparent shear stress, τ', calculated using Equation 2. (c) Estimates of apparent coefficient of friction, μ', calculated from the estimates of τ' using Equation 3. Symbols in black above each histogram show the means and standard deviations of the respective distributions.

2.9 W m^{-1} K^{-1} but if is calculated using the separate expressions of Furlong and Chapman (2013) for upper and lower crust, $\overline{K}$ drops to 2.6 W m^{-1} K^{-1}. Few of the measurements of Whittington et al. (2009) are more conductive than given by their expression, so we presume that the estimate of $\overline{K} = 2.9$ W m^{-1} K^{-1} lies close to the upper bound on average conductivity; see also Robertson (1988, Figure 15) for further evidence on the thermal conductivity of felsic rocks of the upper continental crust. To avoid spurious precision, we round the upper bound on average conductivity to 3 W m^{-1} K^{-1}, and adopt a lower bound of 2.5 W m^{-1} K^{-1}, obtained using the expressions of Furlong and Chapman (2013) for the whole crust.

The divisors S_Q, S_τ, S_A in Equations 1 and 2 additionally depend on thermal diffusivity, convergence rate and the cosine of the dip of the slab beneath the measurement point (Equations A2, A10, and A12). We assign a value of 10^{-6} m^2 s^{-1} to the diffusivity at the top of the lower plate, κ, based on the model of Xu et al. (2004) for the diffusivity of the upper mantle; this estimate is uncertain by perhaps 10% (see England, 2018; Appendix A for discussion). Uncertainties in convergence rate are of order a few percent, and are negligible in comparison with the other uncertainties.

3.3. Estimates of Shear Stress and Temperature at 50–70 km on the Plate Interface

We exclude the two outlying measurements of $Q_S > 80$ mW m^{-2} in Figure 2b. For each of the remaining 20 sites, we estimate apparent stress, τ', and temperature, T_f, on the plate interface beneath the measurement using Equations 1 and 2. We treat the uncertainties discussed in Section 3.2.2 by performing the calculation for each site 10,000 times with random choices of Q_S and z_f from Gaussian distributions given by their published uncertainties (Hayes, 2018; Hayes et al., 2018; Matsumoto et al., 2022), and with random choices of Q_A assuming that it is uniformly distributed between 20 and 40 mW m^{-2} (Section 3.2.2).

The resulting distributions of estimates of temperature on the interface, T_f, apparent stress, τ', and apparent coefficient of friction, μ', are shown in Figure 4. The mean of the 20 estimates of temperature is 660°C, with a standard deviation of 250°C (Figure 4a). The value of average conductivity, $\overline{K}$, that we use for the upper plate is unlikely to be a significant overestimate (see Section 3.2.2); if temperatures were calculated using its lower bound, they would have an average of 800°C. Estimates of τ' are unaffected by uncertainty in thermal conductivity (Equation 2). The mean of the estimates of apparent stress on the interface is 100 MPa, with a standard deviation of 45 MPa (Figure 4b); the corresponding estimates of μ' have a mean of 0.057 and a standard deviation of 0.025 (Figure 4c).

3.4. Comparison With the Kermadec Plate Interface

Uncertainties in heat production and thermal conductivity in the continental setting of Honshu introduce considerable uncertainties in the estimates of shear stress and temperature (Section 3.2.2). It is therefore useful to

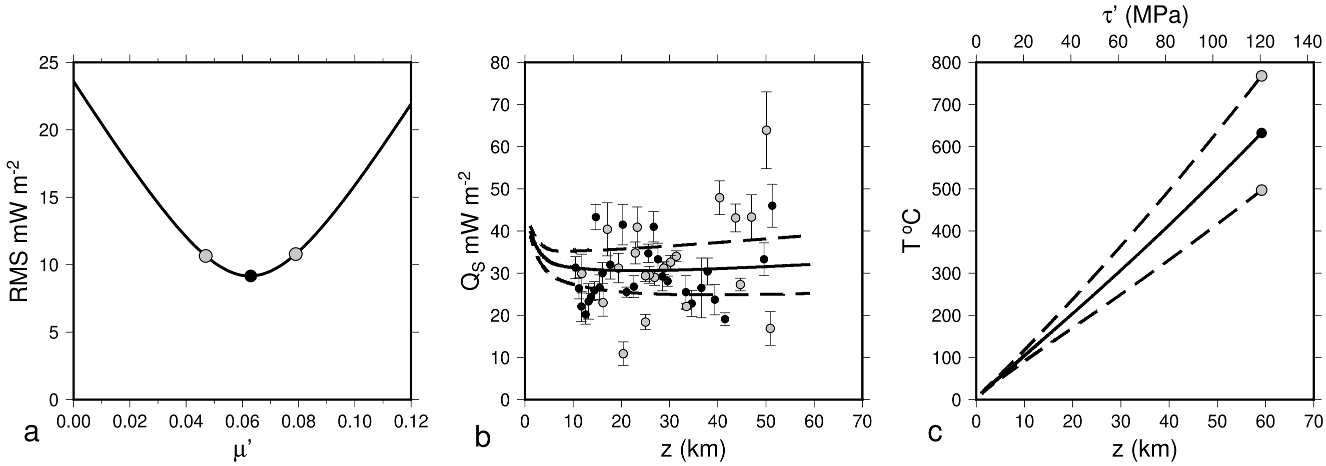

Figure 5. Apparent coefficients of friction and temperatures on the Kermadec plate interface. (a) Variation of root-mean-square (RMS) misfit between observed surface heat flux of Von Herzen et al. (2001), and that calculated from Equations 2 and 3. Solid circle shows minimum RMS misfit, gray circles show values of μ' for which the misfit is greater than the minimum by an amount equal to the average uncertainty in the heat flux measurements. (b) Heat flux observations plotted against depth to the top of the slab beneath measurement site; solid and gray symbols in are for the northern and southern profiles, respectively of Von Herzen et al. (2001). Solid line shows the surface heat flux calculated using the best-fitting value of μ'; dashed lines are calculated using values of μ' shown by the gray circles in (a). (c) Temperature on the plate interface calculated from Equation 1 for the same three values of μ'; upper axis shows shear stress at depth, as given by Equation 3 with the best-fitting value of μ'.

compare the range of estimates for these quantities on the plate interface beneath Honshu with their equivalents derived from an experiment designed to minimize those uncertainties. Von Herzen et al. (2001) estimated shear stress in the oceanic setting of the Kermadec plate boundary, where radiogenic heat production is negligible, and the upper plate consists predominantly of mantle.

We analyze those data taking the conductivity of the upper plate to be that proposed by Xu et al. (2004) for the upper mantle and its density to be 3,300 kg m^{-3}. We determine the coordinates of the top of the slab beneath each measurement of heat flux (u_f, z_f), then find the value of μ' that minimizes the root-mean-square (RMS) difference between the measured heat flux and that calculated from Equation A12 with the values of its parameters appropriate to that point. The minimum misfit is obtained with $\mu' = 0.063$ (Figure 5a). We estimate the uncertainty in μ' by determining the range, centered on the best fit, required to accommodate 68% of the data within their uncertainties, which is $0.05 < \mu' < 0.08$. The shear stress at the maximum depth of thrust faulting in this location (~60 km, (England, 2018, Figure 2)) is 115 ± 25 MPa and the temperature is 630 ± 140°C (Figure 5c).

4. Discussion

4.1. Shear Stress

Several previous studies have estimated shear stresses and/or apparent coefficients of friction on the plate interface beneath northern Honshu. Tichelaar and Ruff (1993) and England (2018) derived estimates of shear stress from analytical expressions, as is done here. Their estimates of μ' lay between 0.03 and 0.12, depending upon their assumed value for Q_A; when their values of Q_A were close to that we use here, their estimates were consistent with ours, as would be expected from the congruity of approaches.

Honda (1985) and Furukawa and Uyeda (1989) used 2D finite-difference models to calculate temperatures in the upper and lower plates, approximating the thermal influence of the mantle wedge by fixing temperatures on its boundaries. Honda (1985) also calculated flow in the mantle wedge, but our remarks are confined to the model used to calculate apparent stresses on the plate interface (Honda, 1985, Figures 11 and 12). Honda (1985) found that, if shear stress on the plate interface is constant, then a level of 50–100 MPa is required for the output of the numerical model to fit the data. If shear stress increases linearly with depth, then a shear stress of 100–250 MPa at a depth of 60 km is required. In contrast, Furukawa and Uyeda (1989) concluded that, if shear stress on the plate boundary increases linearly with depth, then its average value over the plate interface should be no more than 20 MPa. The large discrepancy between these two estimates, made using very similar methods of calculation, arises from different modeling assumptions, as we now discuss.

The calculation of Honda (1985) neglected heat production in the upper plate. If those calculations are adjusted for heat production in the upper plate then stresses are reduced by

$$\Delta\tau \sim \frac{Q_A S_T}{V} \tag{5}$$

(Equation 2). For $Q_A \sim 30$ mW m^{-2} the estimates of shear stress should be reduced by approximately 100 MPa, to 0–150 MPa at a depth of 60 km. This range is equivalent to $0 < \mu' \lesssim 0.08$.

Furukawa and Uyeda (1989) used a value of $Q_A = 30$ mW m^{-2}, as is adopted here, and their calculations were constrained by two heat flux measurement of ~40 mW m^{-2} where the top of the slab reaches a depth of ~60 km (Furukawa & Uyeda, 1989, Figure 12). They estimated that for shear stress increasing linearly with depth the mean stress on the plate interface was 20 MPa (hence 40 MPa at the base); the estimate assuming constant stress was 10 MPa. The data of Matsumoto et al. (2022) suggest that a more appropriate heat-flux constraint would be 60 mW m^{-2} (Figure 2b). The adjustment has the same form as Equation 5, with a change in the surface heat flux replacing that in Q_A. With an increase in heat flux of 20 mW m^{-2} the estimates of stress at 60 km would increase by 60 MPa, to become ~100 and ~70 MPa, with the equivalent range of apparent coefficient of friction being $0.04 \lesssim \mu' \lesssim 0.06$.

Gao and Wang (2014) used a finite-element model to calculate temperatures in upper and lower plates, and to solve for flow and advection of heat in the mantle wedge. They chose a value of $\mu' = 0.025$, but did not specify a range of μ' over which the output of their model agreed with the data. Inspection of the fit between model and data (Gao & Wang, 2014, Figure 2a) suggests that about 70% of the observations are also fit to within error with $\mu' = 0.06$.

Earlier estimates of shear stress on the deeper plate interface beneath northern Honshu ($z_f \gtrsim 50$ km) were constrained by 7 or fewer measurements of heat flux, whereas the estimates here are constrained by 20 such measurements (Figure 2b). When allowance is made for differing assumptions about radiogenic heat production in the upper plate and the constraints imposed by surface heat flux, previous estimates of μ' on the plate interface beneath northern Honshu are consistent with the range found here ($\mu' = 0.06 \pm 0.03$ to one significant figure, Figure 4c).

Von Herzen et al. (2001) used the expressions of Molnar and England (1990) to estimate shear stress on the Kermadec plate interface, assuming it to be planar with a dip of 17 ± 2°, and using a convergence rate of 64 mm/yr from DeMets et al. (1994). They concluded that the heat flux observations are satisfied either by a constant shear stress of ~40 ± 17 MPa or by a linearly increasing shear stress equivalent to $\mu' \sim 0.06 \pm 0.03$ (when their gradient of shear stress with horizontal distance from the trench is converted to the form of Equation 3). Gao and Wang (2014) used the angular velocities of DeMets et al. (2010) and the slab depths of Hayes et al. (2012). They concluded that the measurements may be fit by apparent coefficients of friction in the range $0.04 \leq \mu' \leq 0.1$ with a preferred value of $\mu' = 0.07$. England (2018) used the angular velocities of Argus et al. (2011) and the slab depths of Hayes et al. (2012), but approximating them by a plane, and obtaining ranges of $0.04 \leq \mu' \leq 0.06$ and $0.03 \leq \mu' \leq 0.07$ respectively for the northern and southern profiles of Von Herzen et al. (2001). The range in μ' obtained by these studies is consistent, as discussed in Section 3.2.2 with uncertainty of approximately 10 mW m^{-2} in Q_s that is shown in Figure 5b.

4.2. Temperature at the Seismic-Aseismic Transition on the Plate Interface

Temperatures at the maximum depths of thrust-faulting earthquakes beneath northern Honshu are constrained by heat flux observations to be ~660 ± 250°C. Those temperatures are higher than usually delivered by numerical modeling. For example, Gao and Wang (2014, Figures 2a) and Gao and Wang (2017, Figure 3d) show temperatures, respectively, of ≲400°C and ~300°C in that location, while Syracuse et al. (2010, as reported by van Keken et al. (2011)) calculate ~200°C. Although the range of temperatures we estimate overlaps with the model of Gao and Wang (2014) it does not accommodate the lower temperatures calculated by Syracuse et al. (2010). Equally, the temperature estimate at the maximum depth of thrust-faulting on the Kermadec plate boundary, ~630 ± 140°C, is incompatible with the models of Gao and Wang (2014) (~450°C) and Syracuse et al. (2010) (~250°C).

The differences between the temperatures we calculate from the heat flux data and those derived from the numerical models result from assumptions about the strength of the interface. Syracuse et al. (2010) assumed there to be no shear heating on the plate interface. Gao and Wang (2014, 2017) allowed heating by a combination of

10.1029/2023GC011285

frictional sliding with viscous dissipation in a shear zone whose rheological parameters were designed to represent a quartz-rich fault zone; once temperatures on the interface exceed ∼300–400°C, viscous deformation dominates and shear stresses on the interface drop, hence the rate of temperature increase with depth decreases (Gao & Wang, 2014, Figures 2 and S1–S7). It is not clear that quartz is a common strength-controlling component of plate interfaces (Smye & England, 2023, Figures 9 and 10) and, although the rheological parameters of the minerals most relevant to plate interfaces are very poorly constrained (e.g., discussion of Figure 16, Smye & England, 2023) it is plausible that many of the common metasedimentary and metavolcanic rocks can support shear stresses of order 100 MPa to temperatures of 600°C or higher (Smye & England, 2023, Figures 17–19).

4.3. Comparison With the Geological Record of the Subduction Interface in Japan

Metamorphic belts that are interpreted to have formed on subduction interfaces typically record pressures of $1-2$ GPa (e.g., Ernst, 1973; Miyashiro, 1972; Peacock, 1992; Penniston-Dorland et al., 2015), which span the range of maximum depths of thrust-faulting earthquakes in subduction zones ($\sim30-70$ km, e.g. Hayes et al., 2012, 2018; Heuret et al., 2011). Petrological and microstructural studies of the constituent rocks of those belts may be used to infer temperature, pressure, shear stress, and deformation mechanisms along present-day subduction interface, provided that past metamorphic pressure-temperature conditions can be mapped onto their equivalents in present-day subduction interfaces. That mapping requires independent constraints on the age and dip of the subducting plate and on the convergence rate, which are not usually available. The Cretaceous Sanbagawa belt of SW Japan provides an exception in having useful constraints on both the slab age (60 Myr, see discussion in Ishii & Wallis, 2020) and convergence rate ($\sim200-240$ mm/yr Engebretson et al., 1985).

Figure 6 shows pressure-temperature conditions for the Sanbagawa belt, reported by Enami (1983), Enami et al. (1994), Endo et al. (2009, 2013), Kabir and Takasu (2016), Kouketsu et al. (2021), and Weller et al. (2015) (see Ishii & Wallis, 2020, for further discussion of the metamorphic data). Temperatures at pressures up to ∼1 GPa increase with depth, as would be expected on the plate interface (Equation A1). Above ∼1 GPa, temperatures are almost independent of depth, which is characteristic of the lowest part of the plate interface or the upper part of the wedge-slab interface (e.g., Ishii & Wallis, 2020; England & Smye, 2023).

We compare the metamorphic data obtained from the Sanbagawa belt with thermal profiles calculated using the shear stresses constrained by the heat flux measurements presented here. The shape of the top of the slab on which the Sanbagawa belt formed is unknowable, and we calculate the temperature distribution using the shape of the present-day interface beneath northern Honshu, as described in Appendix B. We have investigated other shapes of plate interface, including that of the present-day Tonga plate interface, which is the only major present-day interface with a convergence rate of ∼200 mm/yr. We found that the temperatures are not sensitive to differences in the shape of the slab, depending principally on convergence rate and the location of the base of the plate interface. The effective coefficient of friction, μ' is 0.06, similar to that determined here from measurements of surface heat flux, and the associated dissipative heating ceases at a depth of 30 km, which is the maximum depth of thrust faulting in the equivalent part of the present-day Tonga plate interface (Hayes et al., 2018).

The obliquity of convergence, in the region that is now SW Japan, was probably between 30° and 60° (Wallis et al., 2009), corresponding to descent speeds, V_n, between ∼170 and 120 mm/yr. For fixed convergence rate, decreasing V_n corresponds to increasing duration of heating on the interface, hence higher temperature at a given depth (Equations A1–A3). If V_n varies between 120 and 240 mm/yr, temperatures on the plate interface vary by no more than ±100°C (Figure 6a). Temperatures on the wedge-slab interface depend weakly on convergence rate, as discussed by England and Katz (2010, Figure 2) and England and Smye (2023, Section 3.2.2). It is beyond the scope of this paper to determine the full range of convergence velocity, obliquity, shear stress, and depth of plate interface that would yield calculated temperature profiles consistent with the P-T conditions preserved in the Cretaceous Sanbagawa belt but it is evident from Figure 6b that an effective coefficient of friction appreciably smaller than the $\mu' \sim 0.06$ that is measured on the present-day interface beneath northern Honshu could not generate the conditions observed in the Sanbagawa belt.

5. Conclusions

Borehole heat flux measurements (Matsumoto et al., 2022) yield estimates of 100 ± 45 MPa for the apparent shear stress (the average stress during slip) at the maximum depth of thrust faulting on the plate interface beneath northern Honshu; those data also constrain the temperature at that depth to be 660 ± 250°C (Section 3.3).

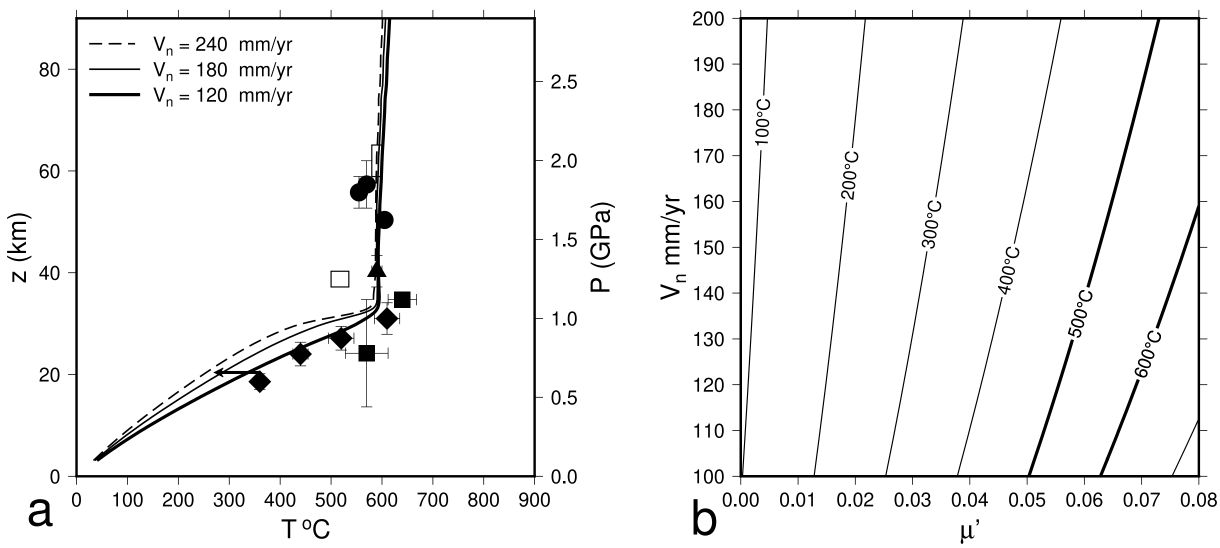

Figure 6. Pressure-temperature (P-T) data from the ∼90-Ma Sanbagawa metamorphism compared with temperature profiles calculated on the basis of shear stress estimates obtained in the present study; pressures are related to depth using a density of 3.1 Mg m^{-3} for the upper plate. (a) P-T conditions for the plate interface at 30 km and shallower are indicated by diamonds (after Enami, 1983; Enami et al., 1994; Kouketsu et al., 2021); arrow on the lowest estimate of temperature indicates that this is an upper bound. Temperatures at pressures above 1 GPa are from (Endo et al., 2009, squares with error bars) (Endo et al., 2013, triangles) (Kabir & Takasu, 2016, ranges indicated by boxes), and (Weller et al., 2015, circles). Lines show temperature profiles calculated for an interface having the same shape as the present-day subduction interface beneath NE Japan; $\mu' = 0.06$, but with dissipative heating ceasing at 30 km, which is the maximum depth of thrust faulting on the Tonga plate interface (Hayes et al., 2018). (b) Temperature at a depth of 30 km on the interface calculated using Equation A1 for a range of μ'; the descent speed V_n is allowed to vary while the convergence rate remains at 240 mm/yr. Thicker contours indicate the range of metamorphic temperatures at depth of ∼30 km in (a).

Uncertainty in these quantities arises both from variability in the heat flux measurements and from the difficulty in estimating the contribution of radiogenic heat production to surface heat flux (Section 3.2.2). Our estimate of shear stress on the plate interface is, within uncertainty, consistent with previous estimates (e.g., Furukawa & Uyeda, 1989; Gao & Wang, 2014; Honda, 1985; Tichelaar & Ruff, 1993), once the influences of modeling assumptions are accounted for (Section 4.1).

The estimates of temperature and stress for Honshu are supported by estimates for the Kermadec plate interface (Von Herzen et al., 2001), which are subject to considerably smaller uncertainty, both because heat production in the upper plate there is negligible, and because the configuration of heat flux measurements was specifically designed to determine shear stress on the plate interface. Those measurements yield estimates of shear stress and temperature at the maximum depth of thrust faulting (also about 60 km) that are very similar to those for Honshu (115 ± 25 MPa and 630 ± 140°C, Section 3.4).

The temperatures that we deduce from the heat flux data are incompatible with the predictions of numerical models that assume negligible shear stress on the plate interface (e.g., Syracuse et al., 2010; van Keken et al., 2018). The temperatures are, however, consistent with the pressure-temperature conditions recorded by rocks from the Sanbagawa belt of SW Japan, and many other high-pressure-low-temperature terrains—supporting the suggestions of many authors (e.g., Behr & Bürgmann, 2021; England & Smye, 2023; Ernst, 1971, 1973, 1975; Ernst et al., 2007; Ishii & Wallis, 2020; Kohn et al., 2018; Miyashiro, 1972, 1973; Oxburgh & Turcotte, 1971; Peacock, 1992; Penniston-Dorland et al., 2015, 2018; Smye & England, 2023) that those terrains contain information on conditions at the depths where major earthquakes occur on present-day subduction interfaces.

Appendix A: Mathematical Model

To calculate temperatures on the plate interface, we adapt the analytical approximations of England and May (2021) to take account of radiogenic heat generation in the upper plate. The analysis differs from those of England and May (2021), who neglected heat generation, and of Molnar and England (1990), who assumed a planar interface and used a model in which radiogenic heating decayed exponentially with depth from the surface

10.1029/2023GC011285

within each plate. As discussed by England and May (2021, Sections 2.4 and 2.5), the analytical approximations differ from numerical solutions to the full equations by a few percent, which is negligible in comparison with uncertainties in the physical parameters.

We treat the radiogenic heat as being generated at a constant rate, A, from the surface to a depth D within the upper plate, with no heat generation in the lower plate. The temperature on the interface at depth z_f is

$$T_f = \frac{Q_0\, z_f}{\overline{K} S_Q} + \frac{\tau' V z_f}{\overline{K} S_\tau} + \frac{A\mathcal{D}^2}{2\overline{K} S_A}, \tag{A1}$$

where Q_0 is the surface heat flux appropriate to the age of the lower plate, which is assumed to be oceanic, V is the long-term average rate of slip across the plate boundary (England & May 2021; Molnar & England, 1990). $\overline{K}$ is the appropriately averaged thermal conductivity of the upper plate (e.g., England, 2018; Appendix A, and see below) and $\mathcal{D}$ is the smaller of z_f and D. τ' is the average shear stress during relative motion across the interface, which we treat here as being related to depth by an effective coefficient of friction, μ', so that $\tau' = \mu' g \rho z_f$. Notation is given in Table A1.

Table A1
Notation

Parameter	Definition
A	Volumetric heat generation in upper crust
a, b	Constants describing curvature of plate interface (Equation B1)
D	Thickness of upper crust
$\mathcal{D}$	The smaller of D and z_f
g	Acceleration due to gravity
$\overline{K}$	Average thermal conductivity of upper plate
$k(T)$, $\overline{k}$	Thermal conductivity of a layer within the upper plate, and its average
Q_0	Heat flux out of top of lower plate had it not been subducted
Q_A	Total heat generation per unit surface area of the crust
Q_f	Heat flux out of the top of the lower plate, at $z = z_f$
Q_S	Heat flux out of the top of the upper plate, at $z = 0$
S_Q, S_τ, S_A	Divisors expressing influence of advection
$t = u/V_n$	Time since top of lower plate entered the trench
T	Temperature[a]
T_f	Temperature[a] on the plate interface at depth z_f
u	Distance along interface from trench to z_f
V	Speed of convergence between plates
V_n	Component of V perpendicular to trench
z	Depth measured from the top of the upper plate
z_f	Depth of subduction interface
z_T	Maximum depth of thrust-faulting earthquakes
z_W	Depth of base of the plate interface
δ	Local dip of the interface at depth z_f
κ	Thermal diffusivity
μ'	Apparent coefficient of friction
ρ	Average density of the upper plate
τ'	Average shear stress during slip on plate interface

[a]The Celsius scale is used, and temperature at Earth's surface is approximated as 0°C.

The quantities S_Q and S_τ in the divisors of the terms on the right-hand side of Equation A1 have the form.

$$S_Q = \cos(\delta) + b_Q \frac{z_f}{\sqrt{\kappa t}}, \tag{A2}$$

$$S_\tau = \cos(\delta) + b_\tau \frac{z_f}{\sqrt{\kappa t}}, \tag{A3}$$

where δ is the local dip of the interface, z_f is its depth at the point of interest, κ is thermal diffusivity; $t = u/V_n$ where u is the distance along the interface to the depth z_f and V_n is the component of plate convergence perpendicular to the trench (England & May 2021). The values of b_Q and b_τ are determined by the dependence on time of the contribution to T_f from the individual heat sources acting alone (Molnar & England, 1990). For S_Q, relating to heating from the lower plate, $b_Q = 2/\sqrt{\pi}$, and for S_τ, relating to dissipative heating on the interface, $b_\tau = 15\sqrt{\pi}/16$; these values apply to the deeper parts of plate interfaces that have the form of a parabola, which is a good approximation to most modern plate interfaces (England & May 2021, Figure 2 and Section 2.3).

We now derive S_A. The analytical approximation assumes that lateral diffusion of heat is negligible, and that the temperature at the top of the lower plate increases with time, t, since it started to pass beneath the upper plate as

$$T_f = C\, t^{m/2} \tag{A4}$$

where m is zero or a positive integer.

The heat flux Q_f at the top of the lower plate is.

$$Q_f = -b_m \frac{\overline{K} T_f}{\sqrt{\kappa t}}, \tag{A5}$$

$$\text{where} \qquad b_m = \frac{\Gamma(m/2+1)}{\Gamma(m/2+1/2)} \tag{A6}$$

(Carslaw & Jaeger, 1959, p. 63-4) and (Molnar & England, 1990; Appendix A). If the only source of heat were radiogenic heating in the upper plate, temperatures at depth $z \leq z_f$ would be

$$T(z) = \frac{A\mathcal{D}^2}{2\overline{K}} + \frac{Q_f z}{\overline{K}} \tag{A7}$$

where Q_f is the heat flowing into the base of the upper plate. From Equations A6 and A7.

$$T_f = \frac{A\mathcal{D}^2}{2\overline{K}} - b_A T_f \frac{z_f}{\sqrt{\kappa t}} \tag{A8}$$

$$= \frac{A\mathcal{D}^2}{2\overline{K} S_A} \tag{A9}$$

$$\text{where} \qquad S_A = 1 + b_A \frac{z_f}{\sqrt{\kappa t}}. \tag{A10}$$

When $z < D$, the dependence of T_f on time is not well represented by Equation A4, but at greater depths, $\mathcal{D} = D$ and we make the approximation that the contribution to T_f from radiogenic heating is constant, which is supported by the arguments and numerical calculations of Molnar and England (1990, Figure 6), and van Keken et al. (2019, Supporting Information, Section 2.4, and Figure S2.7). This approximation gives $b_A = 1/\sqrt{\pi}$.

The surface heat flux, Q_S, is the sum of the separate heat sources, Q_0, τ', and $A\mathcal{D}$ minus the fractions of each that flow into the lower plate:

$$Q_S = \frac{Q_0}{S_Q} + \frac{\tau' V}{S_\tau} + A\mathcal{D}\left(1 - \frac{\mathcal{D}}{2z_f}\left(1 - \frac{1}{S_A}\right)\right), \tag{A11}$$

where the last term is obtained by substituting Equation A9 into Equation A5.

The derivation of this appendix assumes a single layer of constant heat production, but it can readily be modified for other functions describing the distribution of heat production (e.g., Molnar & England, 1990; Tichelaar & Ruff, 1993). In the analysis of Section 3 we need to consider heat production in the upper and lower crust. The correct expression for the two-layer case introduces a somewhat cumbersome modification to the second term in the large brackets in Equation A11. Because $\mathcal{D} \ll 2z_f$ for most of the data we analyze, that term is already much smaller than the first term; furthermore, because the heat generation in the lower crust is much smaller than in the upper crust, the difference between the full and approximate expression we use below is negligible in the context of the uncertainties in measurements (Section 3.2.2). We therefore replace $A\mathcal{D}$ in Equation A11 (the total heat production in the single layer) by Q_A which represents the total heat production in the crust:

$$Q_S = \frac{Q_0}{S_Q} + \frac{\tau' V}{S_\tau} + Q_A\left(1 - \frac{\mathcal{D}}{2z_f}\left(1 - \frac{1}{S_A}\right)\right). \tag{A12}$$

Equation A12 gives the expression we use to relate surface heat flux to τ' (Equation 2). Multiplication of Equation A12 by $\overline{K}/z_f$ and substituting gives the expression we use to calculate T_f from surface heat flux (Equation 1).

Appendix B: Numerical Solutions

The numerical solutions used in Figures 3 and 6 are derived from a kinematically driven 2D model of subduction zones (England & May 2021, Appendix) whose configuration is sketched in Figure 1. The depth, z_f, to the top of the descending plate is defined by

$$z_f = ax^2 + bx^4, \tag{B1}$$

where x is horizontal distance from the trench. The constants for Figures 3 and 6 are $a = 1.01 \times 10^{-3}$ km^{-1} and $b = -8.68 \times 10^{-10}$ km^{-3}, with x in km. With these values, Equation B1 fits the slab configuration for the profile of Figure 2a, determined from the data of Hayes et al. (2018), to within a few km.

The mantle above the plate is represented by a fluid layer, whose rheological parameters are those of Karato and Wu (1993) for dry olivine. The uppermost 10 km of this layer are required to be rigid and have zero velocity; motions elsewhere within the layer are driven by the velocity condition at its base. That velocity is set to zero from the surface to the depth of 75 km, below which the base of the fluid layer moves at the same velocity as the lower plate (depth z_W of Figure 1).

Dissipative heating takes place at a rate $V\mu' g\rho z_f$ in a layer of thickness 1 km that is draped over the lower plate from the surface to the maximum depth of thrust-faulting earthquakes in the region, 60 km (depth z_T of Figure 1). In reality, there may be dissipation on the plate interface by, for example, ductile flow or stable sliding, but this is unconstrained by observation so we neglect it. As discussed in Section 3.2.1, there is no need to consider radiogenic heating in this comparison.

We retain the material properties used by England and May (2021), which differ slightly from those in this paper; the conclusions drawn from Figures 3 and 6 are not influenced by the differences. Average density of material overlying the interface is taken to be 3.3 Mg m^{-3}. Thermal conductivity is 3 W m^{-1} K^{-1} and thermal diffusivity is 0.727×10^{-6} m^2 s^{-1}. The other parameters to the calculation are $V = 92$ mm/yr, $V_n = 91$ mm/yr, and $\mu = 0.057$.

Both temperature and flow fields are solved for using a continuous Galerkin finite element (FE) method employing an unstructured mesh of triangles. Details of the calculation scheme are given by England and May (2021, Appendix).

Data Availability Statement

The heat flux data used here are published in Matsumoto et al. (2022). The geochemical data of Ohta et al. (2021) are to be found in the files of size 1.0 and 2.9 MB that can be downloaded from https://gbank.gsj.jp/geochemmap/data/download.htm.

Acknowledgments

PE gratefully acknowledges support from the Leverhulme Foundation Grant EM-2022-070. SW acknowledges support from the JSPS Grants-in-Aid 21H01188 and 21H05202. He also wishes to thank Y. Tanaka of the University of Tokyo and K. Miyazaki of AIST for helpful discussions. We thank Dave May for providing the code used in calculating the thermal profiles of Figures 3 and 6. We thank K. Wang and S. Schmalholz for valuable reviews.

References

Abercrombie, R. E., & Rice, J. R. (2005). Can observations of earthquake scaling constrain slip weakening? *Geophysical Journal International*, *162*(2), 406–424. https://doi.org/10.1111/j.1365-246x.2005.02579.x

Antriasian, A., Harris, R. N., Trehu, A. M., Henrys, S. A., Phrampus, B. J., Lauer, R., et al. (2019). Thermal regime of the northern Hikurangi Margin, New Zealand. *Geophysical Journal International*, *216*, 1177–1190. https://doi.org/10.1093/gji/ggy450

Argus, D. F., Gordon, R. G., & DeMets, C. (2011). Geologically current motion of 56 plates relative to the no-net-rotation reference frame. *Geochemistry, Geophysics, Geosystems*, *12*(11), Q11001. https://doi.org/10.1029/2011gc003751

Bassett, D., & Watts, A. B. (2015). Gravity anomalies, crustal structure, and seismicity at subduction zones: 1. Seafloor roughness and subducting relief. *Geochemistry, Geophysics, Geosystems*, *16*(5), 1508–1540. https://doi.org/10.1002/2014GC005684

Behr, W. M., & Bürgmann, R. (2021). What's down there? The structures, materials and environment of deep-seated slow slip and tremor. *Philosophical Transactions of the Royal Society A: Mathematical, Physical & Engineering Sciences*, *379*(2193), 20200218. https://doi.org/10.1098/rsta.2020.0218

Brantut, N., & Rice, J. R. (2011). How pore fluid pressurization influences crack tip processes during dynamic rupture. *Geophysical Research Letters*, *38*(24), L24314. https://doi.org/10.1029/2011GL050044

Carslaw, H. S., & Jaeger, J. C. (1959). *Conduction of heat in solids* (2nd ed.). Oxford University Press.

Chi, W. C., & Reed, D. L. (2008). Evolution of shallow, crustal thermal structure from subduction to collision: An example from Taiwan. *Geological Society of America Bulletin*, *120*(5–6), 679–690. https://doi.org/10.1130/B26210.1

DeMets, C., Gordon, R., Argus, D., & Stein, S. (1994). Effect of recent revisions to the geomagnetic reversal time scale on estimates of current plate motions. *Geophysical Research Letters*, *21*(20), 2191–2194. https://doi.org/10.1029/94gl02118

DeMets, C., Gordon, R. G., & Argus, D. F. (2010). Geologically current plate motions. *Geophysical Journal International*, *181*, 1–80. https://doi.org/10.1111/j.1365-246x.2009.04491.x

Dziewonski, A. M., Chou, T.-A., & Woodhouse, J. H. (1981). Determination of earthquake source parameters from waveform data for studies of global and regional seismicity. *Journal of Geophysical Research*, *86*(B4), 2825–2852. https://doi.org/10.1029/jb086ib04p02825

Ekström, G., Nettles, M., & Dziewonski, A. (2012). The global CMT project 2004–2010: Centroid-moment tensors for 13,017 earthquakes. *Physics of the Earth and Planetary Interiors*, *200–201*, 1–9. https://doi.org/10.1016/j.pepi.2012.04.002

Enami, M. (1983). Petrology of pelitic schists in the oligoclase-biotite zone of the Sanbagawa metamorphic terrain, Japan: Phase equilibria in the highest grade zone of a high-pressure intermediate type of metamorphic belt. *Journal of Metamorphic Geology*, *1*(2), 141–161. https://doi.org/10.1111/j.1525-1314.1983.tb00269.x

Enami, M., Wallis, S. R., & Banno, Y. (1994). Paragenesis of sodic pyroxene-bearing quartz schists: Implications for the P-T history of the Sanbagawa belt. *Contributions to Mineralogy and Petrology*, *116*(1–2), 182–198. https://doi.org/10.1007/BF00310699

Endo, S., Nowak, I., & Wallis, S. R. (2013). High-pressure garnet amphibolite from the Funaokayama unit, western Kii Peninsula and the extent of eclogite facies metamorphism in the Sanbagawa belt. *Journal of Mineralogical and Petrological Sciences*, *108*(4), 189–200. https://doi.org/10.2465/jmps.121125

Endo, S., Wallis, S., Hirata, T., Anczkiewicz, R., Platt, J., Thirlwall, M., & Asahara, Y. (2009). Age and early metamorphic history of the Sanbagawa belt: Lu-Hf and *P-T* constraints from the western Iratsu eclogite. *Journal of Metamorphic Geology*, *27*(5), 371–384. https://doi.org/10.1111/j.1525-1314.2009.00821.x

Engdahl, E. R., Di Giacomo, D., Sakarya, B., Gkarlaouni, C. G., Harris, J., & Storchak, D. A. (2020). ISC-EHB 1964–2016, an improved data set for studies of Earth structure and global seismicity. *Earth and Space Science*, *7*(1). https://doi.org/10.1029/2019EA000897

Engebretson, D. C., Cox, A., & Gordon, R. G. (1985). Relative motions between oceanic and continental plates in the Pacific Basin. *Special Papers - Geological Society of America*, *206*, 59.

England, P. C. (2018). On shear stresses and the maximum magnitudes of earthquakes at convergent plate boundaries. *Journal of Geophysical Research*, *123*(8), 7165–7202. https://doi.org/10.1029/2018JB015907

England, P. C., & Katz, R. F. (2010). Melting above the anhydrous solidus controls the location of volcanic arcs. *Nature*, *467*(7316), 700–703. https://doi.org/10.1038/nature09417

England, P. C., & May, D. A. (2021). The global range of temperatures on convergent plate interfaces. *Geochemistry, Geophysics, Geosystems*, *22*(8), e2021GC009849. https://doi.org/10.1029/2021GC009849

England, P. C., & Smye, A. J. (2023). Metamorphism and deformation on subduction interfaces: 1. Physical framework. *Geochemistry, Geophysics, Geosystems*, *24*, e2022GC010644. https://doi.org/10.1029/2022GC010644

Ernst, W. G. (1971). Do mineral parageneses reflect unusually high-pressure conditions of Franciscan metamorphism? *American Journal of Science*, *270*(2), 81–108. https://doi.org/10.2475/ajs.270.2.81

Ernst, W. G. (1973). Blueschist metamorphism and P-T regimes in active subduction zones. *Tectonophysics*, *17*(3), 255–272. https://doi.org/10.1016/0040-1951(73)90006-1

Ernst, W. G. (1975). Systematics of large-scale tectonics and age progressions in Alpine and Circum-Pacific blueschist belts. *Tectonophysics*, *26*(3–4), 229–246. https://doi.org/10.1016/0040-1951(75)90092-X

Ernst, W. G., Hacker, B., & Liou, J. (2007). Petrotectonics of ultrahigh-pressure crustal and upper-mantle rocks—Implications for phanerozoic collisional orogens. In *Special paper 433: Whence the mountains? Inquiries into the evolution of orogenic systems: A volume in honor of Raymond A. Price* (Vol. 433, pp. 27–49). Geological Society of America. https://doi.org/10.1130/2007.2433(02

Furlong, K. P., & Chapman, D. S. (2013). Heat flow, heat generation, and the thermal state of the lithosphere. *Annual Review of Earth and Planetary Sciences*, *41*(1), 385–410. https://doi.org/10.1146/annurev.earth.031208.100051

Furukawa, Y., & Uyeda, S. (1989). Thermal state under the Tohoko arc with consideration of crustal heat generation. *Tectonophysics*, *164*(2–4), 175–187. https://doi.org/10.1016/0040-1951(89)90011-5

Gao, X., & Wang, K. (2014). Strength of stick-slip and creeping subduction megathrusts from heat flow observations. *Science*, *345*(6200), 1038–1041. https://doi.org/10.1126/science.1255487

Gao, X., & Wang, K. (2017). Rheological separation of the megathrust seismogenic zone and episodic tremor and slip. *Nature*, *543*(7645), 416–419. https://doi.org/10.1038/nature21389

Garagash, D. I. (2012). Seismic and aseismic slip pulses driven by thermal pressurization of pore fluid. *Journal of Geophysical Research*, *117*(B4), B04314. https://doi.org/10.1029/2011jb008889

Hamamoto, H., Yamano, M., Goto, S., Kinoshita, M., Fujino, K., & Wang, K. (2011). Heat flow distribution and thermal structure of the Nankai subduction zone off the Kii Peninsula. *Geochemistry, Geophysics, Geosystems*, *12*(10), Q0AD20. https://doi.org/10.1029/2011gc003623

Hayes, G., Moore, G. L., Portner, D. E., Hearne, M., Flamme, H., Furtney, M., & Smoczyk, G. M. (2018). Slab2—A comprehensive subduction zone geometry model [Dataset]. U.S. Geological Survey data release, *362*, 58–61. https://doi.org/10.5066/F7PV6JNV

Hayes, G. P., Moore, G. L., Portner, D. E., Hearne, M., Flamme, H., Furtney, M., & Smoczyk, G. M. (2018). Slab2, a comprehensive subduction zone geometry model. *Science*, *362*(6410), 58–61. https://doi.org/10.1126/science.aat4723

Hayes, G. P., Wald, D. J., & Johnson, R. L. (2012). Slab1.0: A three-dimensional model of global subduction zone geometries. *Journal of Geophysical Research*, *117*(B1), B01302. https://doi.org/10.1029/2011jb008524

Heuret, A., Lallemand, S., Funiciello, F., Piromallo, C., & Faccenna, C. (2011). Physical characteristics of subduction interface type seismogenic zones revisited. *Geochemistry, Geophysics, Geosystems*, *12*(1), Q01004. https://doi.org/10.1029/2010GC003230

Honda, S. (1985). Thermal structure beneath Tohoku northeast Japan. *Tectonophysics*, *112*(1–4), 69–102. https://doi.org/10.1016/0040-1951(85)90173-8

Ishii, K., & Wallis, S. R. (2020). High- and low-stress subduction zones recognized in the rock record. *Earth and Planetary Science Letters*, *531*, 115935. https://doi.org/10.1016/j.epsl.2019.115935

Iwasaki, T., Kato, W., Moriya, T., Hasemi, A., Umino, N., Okada, T., et al. (2001). Extensional structure in Northern Honshu Arc as inferred from seismic refraction/wide-angle reflection profiling. *Geophysical Research Letters*, *28*(12), 2329–2332. https://doi.org/10.1029/2000GL012783

Iwasaki, T., Yoshii, T., Moriya, T., Kobayashi, A., Nishiwaki, M., Tsutsui, T., et al. (1994). Precise P and S wave velocity structures in the Kitakami Massif, Northern Honshu, Japan, from a seismic refraction experiment. *Journal of Geophysical Research*, *99*(B11), 22187–22204. https://doi.org/10.1029/94JB00732

Kabir, M. F., & Takasu, A. (2016). Jadeite-garnet glaucophane schists in the Bizan area, Sambagawa metamorphic belt, eastern Shikoku, Japan: Significance and extent of eclogite facies metamorphism. *Journal of Metamorphic Geology*, *34*(9), 893–916. https://doi.org/10.1111/jmg.12198

Karato, S., & Wu, P. (1993). Rheology of the upper mantle—A synthesis. *Science*, *260*(5109), 771–778. https://doi.org/10.1126/science.260.5109.771

Kohn, M. J., Castro, A. E., Kerswell, B. C., Ranero, C. R., & Spear, F. S. (2018). Shear heating reconciles thermal models with the metamorphic rock record of subduction. *Proceedings of the National Academy of Sciences of the United States of America*, *115*(46), 11706–11711. https://doi.org/10.1073/pnas.1809962115

Kouketsu, Y., Sadamoto, K., Umeda, H., Kawahara, H., Nagaya, T., Taguchi, T., et al. (2021). Thermal structure in subducted units from continental Moho depths in a palaeo subduction zone, the Asemigawa region of the Sanbagawa metamorphic belt, SW Japan. *Journal of Metamorphic Geology*, *39*(6), 727–749. https://doi.org/10.1111/jmg.12584

Lambert, V., Lapusta, N., & Perry, S. (2021). Propagation of large earthquakes as self-healing pulses or mild cracks. *Nature*, *591*(7849), 252–258. https://doi.org/10.1038/s41586-021-03248-1

Lay, T., Kanamori, H., Ammon, C. J., Koper, K. D., Hutko, A. R., Ye, L., et al. (2012). Depth-varying rupture properties of subduction zone megathrust faults. *Journal of Geophysical Research*, *117*(B4), B04311. https://doi.org/10.1029/2011jb009133

Matsubara, M., Sato, H., Uehira, K., Mochizuki, M., & Kanazawa, T. (2017). Three-dimensional seismic velocity structure beneath Japanese islands and surroundings based on NIED seismic networks using both inland and offshore events. *Journal of Disaster Research*, *12*(5), 844–857. https://doi.org/10.20965/jdr.2017.p0844

Matsumoto, T., Yamada, R., & Iizuka, S. (2022). Heat flow data and thermal structure in northeastern Japan. *Earth Planets and Space*, *74*(1), 155. https://doi.org/10.1186/s40623-022-01704-4

McCaffrey, R., Wallace, L., & Beavan, J. (2008). Slow slip and frictional transition at low temperature at the Hikurangi subduction zone. *Nature Geoscience*, *1*(5), 316–320. https://doi.org/10.1038/ngeo178

Miyashiro, A. (1972). Metamorphism and related magmatism in plate tectonics. *American Journal of Science*, *272*(7), 629–656. https://doi.org/10.2475/ajs.272.7.629

Miyashiro, A. (1973). Paired and unpaired metamorphic belts. *Tectonophysics*, *17*(3), 241–254. https://doi.org/10.1016/0040-1951(73)90005-x

Molnar, P., & England, P. (1990). Temperatures, heat flux, and frictional stress near major thrust faults. *Journal of Geophysical Research*, *95*(B4), 4833–4856. https://doi.org/10.1029/jb095ib04p04833

Nishimoto, S., Ishikawa, M., Arima, M., & Yoshida, T. (2005). Laboratory measurement of P-wave velocity in crustal and upper mantle xenoliths from Ichino-megata, NE Japan: Ultrabasic hydrous lower crust beneath the NE Honshu arc. *Tectonophysics*, *396*(3–4), 245–259. https://doi.org/10.1016/j.tecto.2004.12.010

Ohta, A., Imai, N., Okai, T., Manaka, M., Kubota, R., Nakamura, A., & Tachibana, Y. (2021). Watershed analysis for geochemical mapping in Japan based on a hydrologic model: The concentrations of 53 elements and the dominant lithology in a drainage basin. *Geochemical Journal*, *55*(2), 59–88. https://doi.org/10.2343/geochemj.2.0618

Oxburgh, E. R., & Turcotte, D. L. (1971). Origin of paired metamorphic belts and crustal dilation in island arc regions. *Journal of Geophysical Research*, *76*(5), 1315–1327. https://doi.org/10.1029/jb076i005p01315

Parsons, B., & Sclater, J. G. (1977). An analysis of the variation of ocean floor bathymetry and heat flow with age. *Journal of Geophysical Research*, *82*(5), 802–827. https://doi.org/10.1029/jb082i005p00803

Peacock, S. M. (1992). Blueschist-facies metamorphism, shear heating, and P-T-t paths in subduction shear zones. *Journal of Geophysical Research*, *97*(B12), 17693–17707. https://doi.org/10.1029/92jb01768

Penniston-Dorland, S. C., Kohn, M. J., & Manning, C. E. (2015). The global range of subduction zone thermal structures from exhumed blueschists and eclogites: Rocks are hotter than models. *Earth and Planetary Science Letters*, *428*, 243–254. https://doi.org/10.1016/j.epsl.2015.07.031

Penniston-Dorland, S. C., Kohn, M. J., & Piccoli, P. M. (2018). A mélange of subduction temperatures: Evidence from Zr-in-rutile thermometry for strengthening of the subduction interface. *Earth and Planetary Science Letters*, *482*, 525–535. https://doi.org/10.1016/j.epsl.2017.11.005

Rice, J. R. (2006). Heating and weakening of faults during earthquake slip. *Journal of Geophysical Research*, *111*(B5), 29. https://doi.org/10.1029/2005jb004006

Robertson, E. R. (1988). *Thermal properties of rocks, open-file report*. United States Department of the Interior, series: Open-File Report.

Rudnick, R. L., & Gao, S. (2003). Composition of the continental crust. In R. L. Rudnick (Ed.), *The crust*, *Treatise on geochemistry* (Vol. 3). Elsevier.

Ruedas, T. (2017). Radioactive heat production of six geologically important nuclides. *Geochemistry, Geophysics, Geosystems*, *18*(9), 3530–3541. https://doi.org/10.1002/2017GC006997

Scholz, C. H., & Campos, J. (2012). The seismic coupling of subduction zones revisited. *Journal of Geophysical Research*, *117*(B5), B05310. https://doi.org/10.1029/2011jb009003

Segall, P., & Bradley, A. M. (2012). The role of thermal pressurization and dilatancy in controlling the rate of fault slip. *Journal of Applied Mechanics*, *79*(3). https://doi.org/10.1115/1.4005896

Shreve, R. L., & Cloos, M. (1986). Dynamics of sediment subduction, melange formation, and prism accretion. *Journal of Geophysical Research*, *91*(B10), 10229–10245. https://doi.org/10.1029/jb091ib10p10229

Smye, A. J., & England, P. C. (2023). Metamorphism and deformation on subduction interfaces: 2. Petrological and tectonic implications. *Geochemistry, Geophysics, Geosystems*, *24*(1), e2022GC010645. https://doi.org/10.1029/2022GC010645

Syracuse, E. M., Keken, P. E. V., & Abers, G. A. (2010). The global range of subduction zone thermal models. *Physics of the Earth and Planetary Interiors*, *183*(1–2), 73–90. https://doi.org/10.1016/j.pepi.2010.02.004

Tanaka, A., Yamano, M., Yano, Y., & Sasada, M. (2004). Geothermal gradient and heat flow data in and around Japan (I): Appraisal of heat flow from geothermal gradient data. *Earth Planets and Space*, *56*(12), 1191–1194. https://doi.org/10.1186/bf03353339

Tichelaar, B. W., & Ruff, L. (1993). Depth of seismic coupling along subduction zones. *Journal of Geophysical Research*, *98*(B2), 2017–2037. https://doi.org/10.1029/92jb02045

van Keken, P. E., Hacker, B. R., Syracuse, E. M., & Abers, G. A. (2011). Subduction factory: 4. Depth-Dependent flux of H_2O from subducting slabs worldwide. *Journal of Geophysical Research*, *116*(B01), 401–415.

van Keken, P. E., Wada, I., Abers, G. A., Hacker, B. R., & Wang, K. (2018). Mafic high-pressure rocks are preferentially exhumed from warm subduction settings. *Geochemistry, Geophysics, Geosystems*, *19*(9), 2934–2961. https://doi.org/10.1029/2018gc007624

van Keken, P. E., Wada, I., Sime, N., & Abers, G. A. (2019). Thermal structure of the forearc in subduction zones: A comparison of methodologies. *Geochemistry, Geophysics, Geosystems*, 2019GC008334. https://doi.org/10.1029/2019GC008334

Venzke, E. (2023). *Global volcanism program, 2023. [Database] volcanoes of the world (v. 5.1.1; 17 August 2023)*. Distributed by Smithsonian Institution. https://doi.org/10.5479/si.GVP.VOTW5-2023.5.1

Viesca, R. C., & Garagash, D. I. (2015). Ubiquitous weakening of faults due to thermal pressurization. *Nature Geoscience*, *8*(11), 875–879. https://doi.org/10.1038/ngeo2554

Von Herzen, R., Ruppel, C., Molnar, P., Nettles, M., Nagihara, S., & Ekström, G. (2001). A constraint on the shear stress at the Pacific-Australian plate boundary from heat flow and seismicity at the Kermadec forearc. *Journal of Geophysical Research*, *106*(B4), 6817–6833. https://doi.org/10.1029/2000jb900469

Wada, I., & Wang, K. (2009). Common depth of slab-mantle decoupling: Reconciling diversity and uniformity of subduction zones. *Geochemistry, Geophysics, Geosystems*, *10*, 1–36. https://doi.org/10.1029/2009gc002570

Wallis, S. R., Anczkiewicz, R., Endo, S., Aoya, M., Platt, J. P., Thirlwall, M., & Hirata, T. (2009). Plate movements, ductile deformation and geochronology of the Sanbagawa belt, SW Japan: Tectonic significance of 89–88 Ma Lu-Hf eclogite ages. *Journal of Metamorphic Geology*, *27*(2), 93–105. https://doi.org/10.1111/jmg.2009.27.issue-2

Weller, O. M., Wallis, S. R., Aoya, M., & Nagaya, T. (2015). Phase equilibria modelling of blueschist and eclogite from the Sanbagawa metamorphic belt of southwest Japan reveals along-strike consistency in tectonothermal architecture. *Journal of Metamorphic Geology*, *33*(6), 579–596. https://doi.org/10.1111/jmg.12134

Whittington, A. G., Hofmeister, A. M., & Nabelek, P. I. (2009). Temperature-dependent thermal diffusivity of the Earth's crust and implications for magmatism. *Nature*, *458*(7236), 319–321. https://doi.org/10.1038/nature07818

Xu, Y., Shankland, T. J., Linhardt, S., Rubie, D. C., Langenhorst, F., & Klasinski, K. (2004). Thermal diffusivity and conductivity of olivine, wadsleyite and ringwoodite to 20 GPa and 1373 K. *Physics of the Earth and Planetary Interiors*, *143–144*, 321–336. https://doi.org/10.1016/j.pepi.2004.03.005

Yoshioka, S., Suminokura, Y., Matsumoto, T., & Nakajima, J. (2013). Two-dimensional thermal modeling of subduction of the Philippine Sea plate beneath southwest Japan. *Tectonophysics*, *608*, 1094–1108. https://doi.org/10.1016/j.tecto.2013.07.003